

Rapid morphology characterization of two-dimensional TMDs and lateral heterostructures based on deep learning

Junqi He,^{†,ⓐ} Yujie Zhang,^{†,ⓐ} Jialu Wang,[‡] Tao Wang,[¶] Pan Zhang,[§] Chengjie
Cai,[†] Jinxing Yang,[†] Xiao Lin,^{||,⊥} and Xiaohui Yang^{*,†,#,||}

[†]*Department of Physics, China Jiliang University, Hangzhou 310018, P. R. China*

[‡]*Hangzhou Key Laboratory of Quantum Matter, School of Physics, Hangzhou Normal
University, Hangzhou 311121, China*

[¶]*ZJU-Hangzhou Global Scientific and Technological Innovation Center, College of
Integrated Circuits, Zhejiang University, Hangzhou, 311215, China.*

[§]*Department of Physics and Texas Center for Superconductivity, University of Houston,
Houston, TX 77204, USA*

^{||}*Key Laboratory for Quantum Materials of Zhejiang Province, Department of Physics,
School of Science, Westlake University, Hangzhou 310030, P. R. China*

[⊥]*Institute of Natural Sciences, Westlake Institute for Advanced Study, Hangzhou 310024,
P. R. China*

[#]*Zhejiang Province Key Laboratory of Quantum Technology and Device, Zhejiang
University, Hangzhou 310027, P. R. China*

[ⓐ]*These authors contributed equally to this work.*

E-mail: xiaohuiyang@cjlu.edu.cn

Abstract

Two-dimensional (2D) materials and heterostructures exhibit unique physical properties, necessitating efficient and accurate characterization methods. Leveraging advancements in artificial intelligence, we introduce a deep learning-based method for efficiently characterizing heterostructures and 2D materials, specifically MoS₂-MoSe₂ lateral heterostructures and MoS₂ flakes with varying shapes and thicknesses. By utilizing YOLO models, we achieve an accuracy rate of over 94.67% in identifying these materials. Additionally, we explore the application of transfer learning across different materials, which further enhances model performance. This model exhibits robust generalization and anti-interference ability, ensuring reliable results in diverse scenarios. To facilitate practical use, we have developed an application that enables real-time analysis directly from optical microscope images, making the process significantly faster and more cost-effective than traditional methods. This deep learning-driven approach represents a promising tool for the rapid and accurate characterization of 2D materials, opening new avenues for research and development in material science.

Keywords

2D material, TMDs, lateral heterostructure, deep learning, instance segmentation, morphology characterization

Introduction

Two-dimensional (2D) materials have attracted significant attention due to their excellent mechanical, electrical, thermal, and optical properties, making them ideal candidates for next-generation technologies.¹⁻⁶ Among these, transition metal dichalcogenides (TMDs) such as MoS₂ and MoSe₂ stand out for their tunable bandgaps and strong light-matter interactions.^{3,7-11} The properties of 2D materials are highly sensitive to thickness and morphol-

ogy.^{3,12–15} For example, single-layer MoS₂ has a direct bandgap, making it suitable for optoelectronics, while multilayer MoS₂ switches to an indirect bandgap, altering its electronic behavior.^{3,8,9} The performance of 2D materials also depends on shape and size, with large-area flakes showing superior charge transport properties, while nanostructures with edge defects or vacancies exhibit enhanced catalytic activity.^{12,15–19}

The inherent limitations of individual 2D materials have prompted extensive research into heterostructures, which combine distinct materials to enhance or tailor their properties while preserving the beneficial characteristics of the constituent components.^{20–22} These heterostructures are typically classified as lateral or vertical, with lateral heterostructures offering advantages such as reconfigured band structures, reduced interlayer scattering, and superior optoelectronic performance.^{22–25} Such attributes make lateral heterostructures particularly promising for next-generation technologies in electronics, optoelectronics, and flexible devices.^{26–28} TMD heterostructures, like MoS₂-MoSe₂, have been particularly attractive for semiconductor applications due to their remarkable optoelectronic and thermoelectric properties.^{29–35}

Due to the diverse physical properties, 2D materials and their heterostructures require highly accurate and efficient characterization techniques. Traditional techniques such as atomic force microscopy (AFM) and Raman spectroscopy are effective but time-consuming.^{23,36} In contrast, artificial intelligence, particularly machine learning and deep learning, offers data-driven solutions for efficient material characterization.^{37–44} Models like CNNs, including Mask R-CNN, U-Net, and YOLO, have been used for analyzing optical images of 2D materials, enabling accurate identification of layer thickness, defects, and heterostructures.^{45–50} These methods reduce time and cost compared to traditional measurements and also offer the potential for characterizing physical properties. In the identification of heterostructures, support vector machine (SVM) have been used to distinguish graphene-MoS₂ heterostructures, while artificial neural network (ANN) and conditional generative adversarial network (cGAN) have been applied to identify WS₂-MoS₂ heterostructures.^{50–52} Despite their success,

current approaches face challenges in portability and require extensive dataset preprocessing, with inference results often needing manual validation.

In this study, we propose a deep learning-based approach for the rapid and accurate characterization of MoS₂ flakes and MoS₂-MoSe₂ lateral heterostructures. Using YOLO models (YOLOv8 and YOLOv11) for object detection and instance segmentation, our method surpasses traditional techniques with faster inference, smaller model size, higher accuracy, and reduced data requirements. We synthesized the materials via chemical vapor deposition (CVD) and characterized them using Raman spectroscopy. An annotated optical image dataset was created, achieving over 96% recognition accuracy for heterostructures. We also observed that synthesis conditions significantly affect MoS₂ morphology, which in turn influences its properties. We developed a shape recognition method using deep learning, achieving over 94% accuracy in detecting and quantifying nanoscale shapes. Transfer learning was applied to fine-tune a pre-trained heterostructure model on a MoS₂ thickness dataset, improving performance by 3%. The model also demonstrated robust generalization abilities. To streamline the characterization process, we developed a software tool that integrates deep learning models with optical microscope outputs for real-time inference, reducing processing delays. This approach enhances operational efficiency and highlights the practical applicability of deep learning for large-scale material analysis.

Results and discussion

The experimental process is depicted in Figure 1a. Initially, an optical microscope was utilized to capture a large number of optical images of 2D materials. Lateral heterostructures were characterized using Raman spectroscopy, and the features were annotated based on the characterization results to train them in instance segmentation tasks. The optical images of the shapes were classified into three categories for annotation: dendritic, hexagonal, and triangle. Once the annotation was completed, the object detection task was proceeded

with. Transfer learning was applied to the dataset of material thicknesses, which were classified as thin, thick, and bulk, followed by training for the instance segmentation task. The training process and model architecture are illustrated in Figure 1b. Considering the hardware environment and dataset sizes, only the three smallest YOLO models, namely n, s, and m, were used for training. The difference between them lies in the size of the neural network, with the network becoming progressively deeper and wider from n to m. The models architectures are shown in Supplementary Information Section 1 and 2.

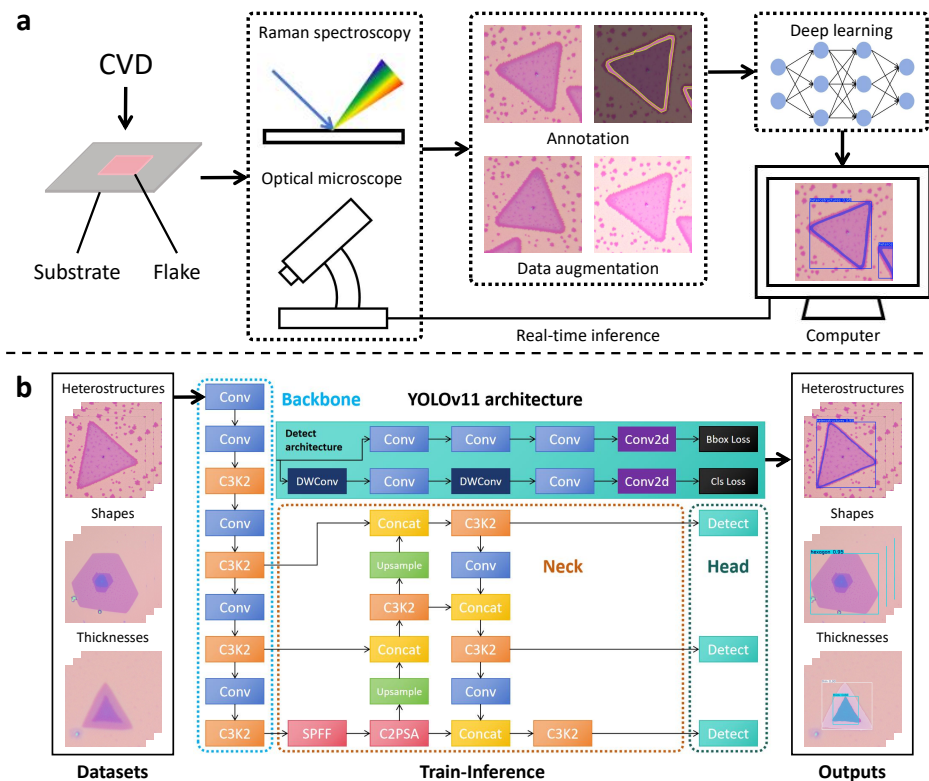


Figure 1: Experimental workflow and deep learning architecture. (a) Key steps: Material preparation → structural characterization → dataset annotation → YOLOv11 training → real-time deployment on optical microscopy systems. (b) YOLOv11 architecture schematic showing data input (left), model architecture (center), and inference results (right).

Training results

The training results for the $\text{MoS}_2\text{-MoSe}_2$ heterostructures dataset are shown in Figure 2. It is evident that the performance indexes of all models are at a relatively high level. Among them,

mAP50 and mAP50-90 are important indicators for evaluating object detection algorithms, representing the overlap between predicted boxes and real boxes. The specific calculation process is shown in the Supplementary Information Section 3. Under the same model size, YOLOv11 outperforms YOLOv8 significantly, with an average improvement of 3.74% in boundary box detection and 6.80% in mask segmentation for mAP. From the perspective of model size analysis, the average improvement in mAP50 for mask segmentation is 3.37% as the model size increases, while the average improvement in mAP50-90 is 17.46% with larger model sizes. Among these, YOLOv8s-seg shows a 21.37% improvement compared to YOLOv8n-seg. This suggests that increasing the model’s complexity can effectively enhance its ability to infer and identify heterostructures. Of all the models, YOLOv11m-seg achieved the best performance. From the confusion matrices (Figure S3), it can be observed that the model’s recognition accuracy exceeds 95.6%, indicating excellent performance.

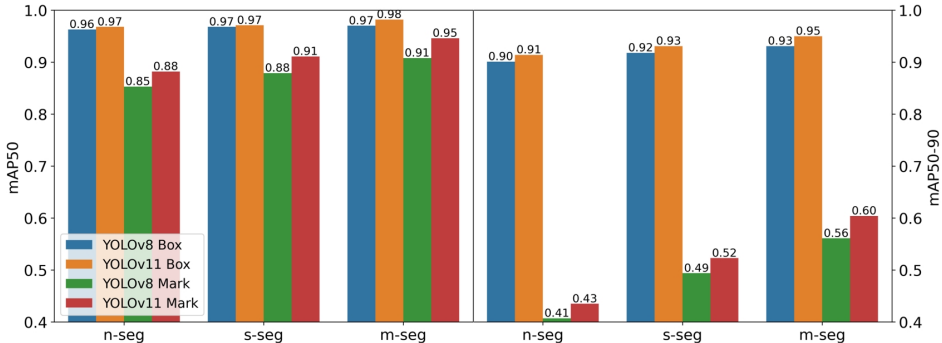


Figure 2: Performance comparison of heterostructure characterization models. Among them, box refers to boundary box detection, and mark refers to mask segmentation. The left image shows mAP50, and the right image shows mAP50-90.

Figure 3 shows the actual inference results of the YOLO model. The morphology of the lateral heterostructures of MoS₂-MoSe₂ was characterized by optical microscopy and Raman spectroscopy. Figure 3a and b present the optical images and corresponding Raman mapping images of the heterostructures, respectively. Figure 3c shows the inference results. The Raman spectra measured at the center, periphery, and boundary areas of the triangle is shown in Figure 3d. The A_{1g} mode (out-of-plane vibration) and E_{2g}^1 mode (in-plane vibration) of MoS₂ appear in the center area, while the A_{1g} mode and E_{2g}^1 mode of MoSe₂

appear in the periphery area. At the junction, four peaks corresponding to the A_{1g} and E_{2g}^1 modes of MoS_2 , as well as the A_{1g} and E_{2g}^1 modes of MoSe_2 , confirm the presence of a lateral heterostructure.⁵³ The Raman mapping characterization in Figure 3b further confirms the coexistence of internal MoS_2 and external MoSe_2 , with clear visibility at the interface, revealing the spatial distribution of heterostructures and indicating the seamless lateral coexistence of two different materials within the same triangular domain.

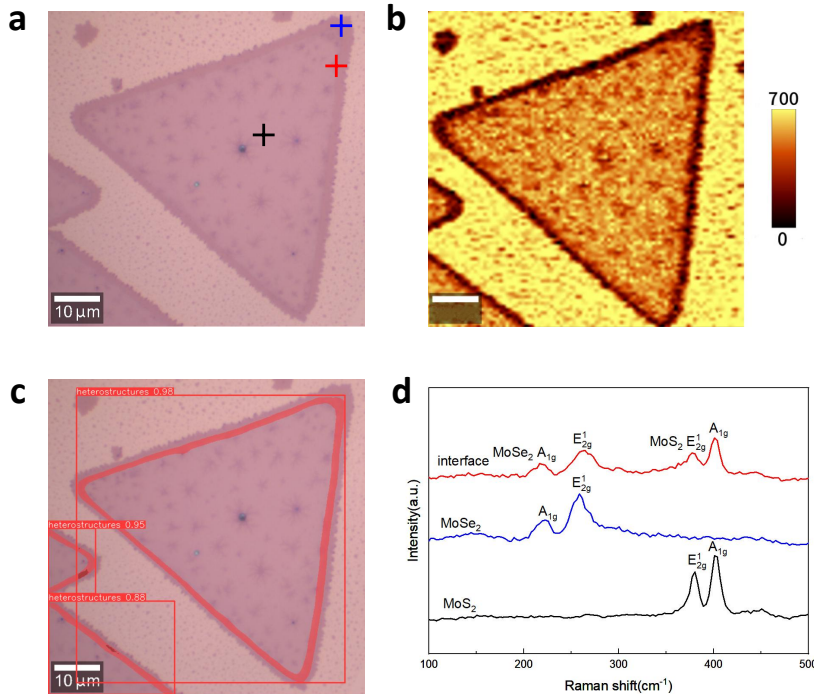


Figure 3: Characterization of lateral heterostructures of MoS_2 - MoSe_2 and YOLO model inference results. (a) Optical images of the heterostructures. (b) Raman mapping of the heterostructures. (c) Heterostructures predicted based on the YOLO model. (d) Raman spectra, where the measurement areas are marked in red, blue, and black in (a).

The morphology and spatial distribution of MoS_2 nanostructures are highly sensitive to synthesis parameters such as growth duration, temperature gradients, precursor stoichiometry, and the positioning of the substrate within the reaction zone.^{54–57} Recent advancements in deep learning-based shape identification techniques facilitate the rapid mapping of synthesis conditions to nanostructure geometries, providing real-time feedback for process optimization. The results of training the shape dataset using YOLOV11 are shown in Table S4-S5. The confusion matrix for YOLOv11s (Figure S4) shows an average recognition accu-

racy of 94.67%. Figures 4a-c display the model’s ability to effectively identify MoS₂ shapes with high confidence. By analyzing the recognized boundary boxes, the area proportions of each shape can be calculated. For example, as shown in Figure 4d, triangles account for 17.60% of the image area, while hexagons cover 4.86%. This rapid identification and statistical method based on deep learning can aid in regulating the growth of MoS₂ or other 2D materials with different shapes at high temperatures.⁵⁸

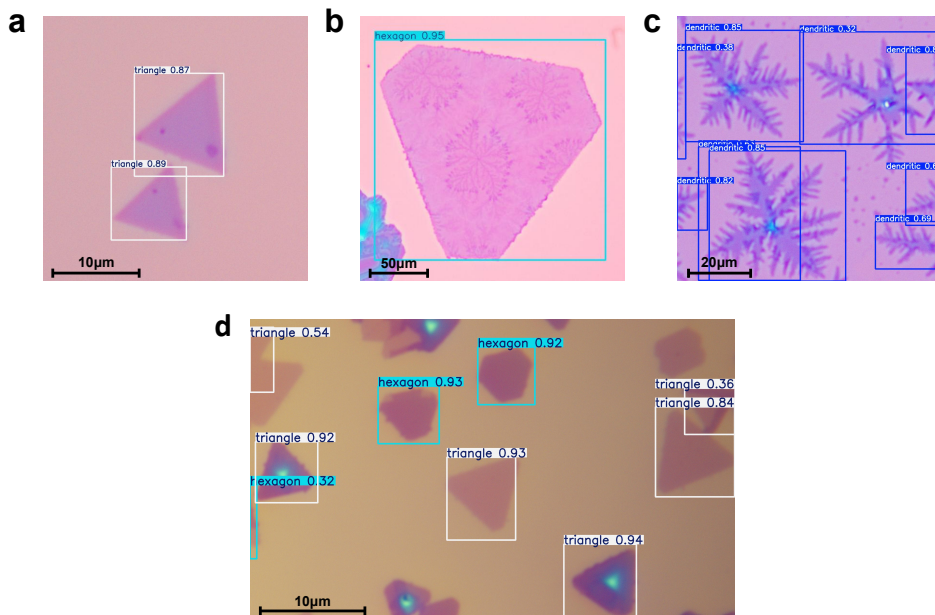


Figure 4: Identification results of MoS₂ with different shapes: (a) triangle, (b) hexagon, (c) dendritic. (d) Optical image inference results of MoS₂.

The YOLOv11 models trained with the heterostructures dataset were used for transfer learning on the thicknesses dataset, with results shown in Table S7. Figure 5a compares the loss curves for direct training and transfer learning with the YOLOv11m-seg model. The transfer learning model shows faster loss reduction, outperforming the original model in the initial phases. After 600 epochs, the loss decreased by 17.84% for the training set and 11.38% for the validation set compared to the original model. Additionally, the transfer learning model excels in performance, as shown in Figure 5b, with better mAP50-90 results. After the 189th and 228th epochs, it surpassed the highest mAP50-90 achieved by the original model in both boundary box detection and mask segmentation. After 600 epochs,

the transfer learning model led by 2.08% in detection boundary box mAP50-90 and 3.90% in mask segmentation mAP50-90. Inference results (Figures 5c-d) for both models were almost identical, but the transfer learning model identified more instances, detecting 3 more bulk instances and 1 more thin instance. The confusion matrix (Figure S5) shows an average accuracy of over 97.3% for both models, but transfer learning achieved this in less than half the training time. Transfer learning was also conducted on the WTe₂ thickness dataset (Figure S6), where it did not significantly improve performance compared to the original model. However, in early training, the loss decreased faster, and mAP50-90 improved more quickly, indicating that transfer learning is less effective across different materials. Overall, transfer learning enhances model performance within the same material, but its impact is less significant when applied between different materials.

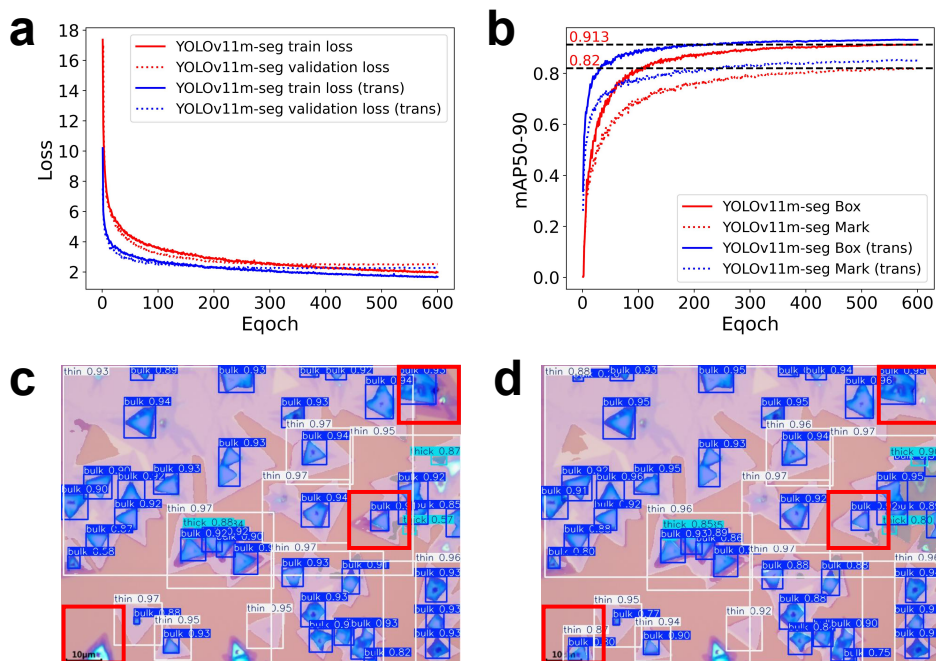


Figure 5: Training results of the MoS₂ thicknesses dataset. (a) Loss curves, where the solid line indicates the training set loss and the dashed line represents the validation set loss. (b) mAP50-90 curves, with the solid line showing the mAP50-90 for the boundary box detection and the dashed line for mask segmentation. In (a) and (b), the red line represents the original model, and blue line denotes the transfer learning model. (c) YOLOv11m-seg model inference results. (d) Inference results of YOLOv11m-seg model after transfer learning. Differences between (c) and (d) are highlighted with red boxes.

environments. The second column of Figure 6 displays inference results for optical images at various magnifications. At different magnifications, the propagation path of light in the microscope varies, leading to light scattering and chromatic aberration. However, the model still maintains strong performance at magnifications of $200\times$, $1000\times$, and $1000\times$, demonstrating effective inference under different lighting conditions.

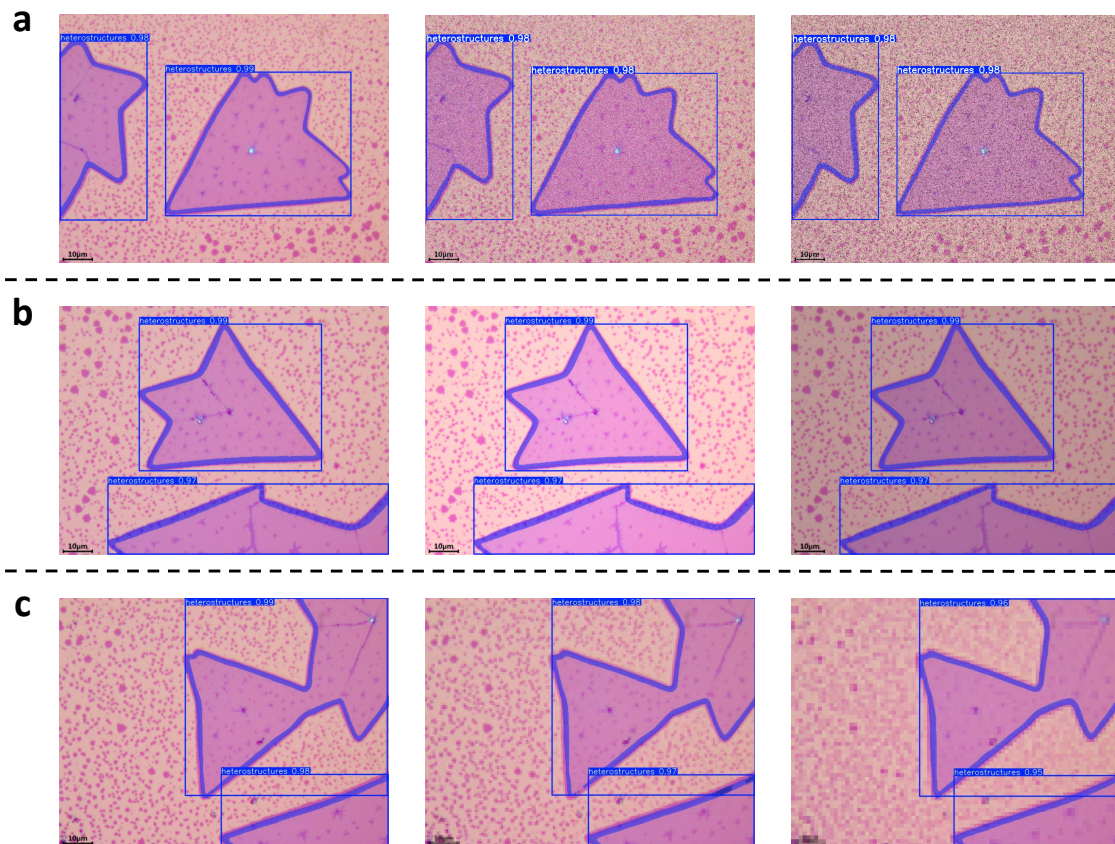


Figure 7: Generalization ability of the YOLO model on anomalous optical images of heterostructures. (a) Robustness to noise: the first image shows the original inference result, the second with 20% Gaussian noise, and the third with 20% salt-and-pepper noise (50% salt, 50% pepper). (b) Sensitivity to brightness: the first image represents the original inference, the second with a 20% brightness increase, and the third with a 20% decrease. (c) Performance at different resolutions: the first image is the original inference, while the second and third correspond to resolution reductions to $1/5$ and $1/10$ of the original, respectively.

Figure 7 shows the generalization ability of the models under three interference factors: noise, brightness, and resolution. It can be observed that the models' inference results under interference are almost identical to the original image, demonstrating strong anti-interference

ability. We conducted separate tests on the characterization of shape and thickness (Figure S7-S8), and the model also demonstrated excellent performance. This indicates all models have good robustness and anti-interference ability.

Application

Optical microscopes can be integrated with deep learning models for real-time inference. we propose a novel method based on YOLO models for real-time inference, implemented using Python. This approach not only achieves high-frame-rate speeds but also supports local deployment, eliminating the time and resource costs of image transmission.

The real-time inference process is shown in Figure 8. It involves capturing the microscope screen using the MSS (Monitor Screen Shots) library, feeding the screenshot into the YOLO model, and outputting the processed image in real-time via OpenCV. The experimental setup is shown in Figure S10, and Supplementary Video 1 demonstrates the real-time inference functionality. Thanks to the efficient YOLO models, we can deploy deep learning locally for real-time processing. Table S10 shows the inference speed and FPS on different computers, with the low-complexity model achieving up to 50 FPS.

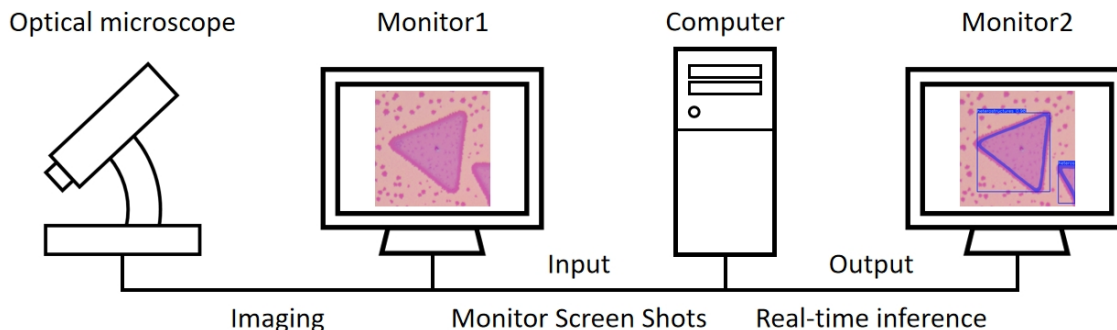


Figure 8: Real-time inference process. Optical images are captured using an optical microscope and transferred to a computer (displayed on Monitor 1). The MSS library then screenshots these images and feeds them into the YOLO model for inference. The results are shown on Monitor 2. By continuously capturing screenshots and running inferences multiple times per second, a real-time video stream is generated.

Conclusions

In summary, this article proposes a novel deep learning-based method for rapidly characterizing MoS₂-MoSe₂ lateral heterostructures. We also use deep learning to characterize the shape and thickness of MoS₂ flakes, and find that transfer learning can effectively enhance accuracy. The experimental results show that the accuracy of heterostructures characterization method reaches 95.6%, with shape recognition accuracy of 94.67% and thickness recognition accuracy of 97.3%. After testing, the trained models demonstrate strong robustness and resistance to interference. Additionally, for convenience in characterization, we integrated optical microscopy with deep learning models to achieve real-time inference. This characterization method based on deep learning provides a faster and more convenient way to characterize the heterostructures and other physical properties of 2D materials.

Methods

Preparation and characterization

The MoS₂ flakes and MoS₂-MoSe₂ lateral heterostructures were synthesized via atmospheric pressure chemical vapor deposition (APCVD) in a dual-temperature zone horizontal tube furnace. MoO₃ powder (Alfa Aesar, 99.998%) mixed with NaCl (Alfa Aesar, 99.99%) was placed in an alumina boat in the high-temperature zone with a SiO₂/Si substrate positioned above it.⁵⁹ Sulfur (Alfa Aesar, 99.999%)(240 °C zone) and selenium powders (Alfa Aesar, 99.999%) were placed in separate upstream alumina boats, with sulfur closer to MoO₃.⁶⁰ The furnace was heated at 25 °C/min under a pure argon flow 120 (standard cubic centimeters per minute (sccm)). After 15 minutes of MoS₂ growth, the atmosphere was switched to N₂/H₂ (9:1) gas mixture for 10 minutes to terminate MoS₂ formation.²⁹ The Se zone temperature was then raised to 350 °C (substrate zone maintained at 650 °C) for 15 minutes for MoSe₂ edge-selective growth under Se vapor. Finally, natural cooling yielded the

heterostructures.^{26,30}

The optical images were acquired using an optical microscope (AOSVI, L100-3M100). Raman spectroscopy was performed using a WITEC alpha 300R micro Raman spectrometer equipped with a 532 nm laser (10 mW power) at room temperature.

Dataset preprocessing

We selected 180 heterostructure images with distinct features, 50 MoS₂ optical images with different shapes, and 50 MoS₂ optical images with different thickness. Split all images into squares of size 640×640. Use the Roboflow online annotation tool for annotation, and save the boundary box coordinates and masks of each instance in YOLO format. Then perform data augmentation on the dataset, as shown in Figure S12, which was expanded to 3955, 1101, and 1103 images, respectively. We divided the datasets into a training set and a validation set in an 8:2 ratio, and used the remaining unselected images as the test sets.

Training environment

Software environment with Python 3.9, PyTorch 2.5.0, and CUDA 11.7. Hardware environment with NVIDIA GeForce RTX 3060 GPU, 64GB memory. The hyperparameters are shown in Table S1, S3, and S6. Real-time inference programs based on Python rely on libraries such as PyQt5, OpenCV, MSS, and PyTorch for implementation. In Supplementary Video 2, all the functions and usage methods of the application are demonstrated.

Acknowledgement

Xiaohui Yang acknowledges the support from the Zhejiang Provincial Natural Science Foundation of China (Grant No. LQ23A040009) and the National Natural Science Foundation of China (Grant No. 12304168). Jialu Wang acknowledges the support from the National Natural Science Foundation of China (Grant No. 12404047).

Data Availability

The datasets used in this study are available from the corresponding author upon reasonable request. The codes underlying this study are openly available in Github at <https://github.com/TripHawkers/OM-real-time-inference>.

Supporting Information Available

- Supplementary Information: Deep learning algorithms, Optimizer, Performance index, Model training results, Generalization ability, Real-time inference, Data augmentation.
- Video 1: real-time inference
- Video 2: application function demonstration

Author Contributions

J.H. and Y.Z. contributed equally to this work. J.H. and X.Y. conceived the project; Y.Z. synthesized the samples and provided optical images with the help of C.C. and J.Y.; Y.Z. performed the Raman measurements with the help J.W. and T.W.; J.H. implemented the software, trained the neural network, and analyzed the results with the help from P.Z.; X.Y. supervised the research program. All authors participated in the discussion of the results and the writing of the manuscript.

Competing interests

The authors declare no competing interests.

References

1. Novoselov, K. S.; Geim, A. K.; Morozov, S. V.; Jiang, D.; Zhang, Y.; Dubonos, S. V.; Grigorieva, I. V.; Firsov, A. A. Electric field effect in atomically thin carbon films. *Science* **2004**, *306*, 666–669.
2. Novoselov, K. S.; Jiang, D.; Schedin, F.; Booth, T. J.; Khotkevich, V. V.; Morozov, S. V.; Geim, A. K. Two-dimensional atomic crystals. *Proc. Natl. Acad. Sci.* **2005**, *102*, 10451–10453.
3. Chhowalla, M.; Shin, H. S.; Eda, G.; Li, L.-J.; Loh, K. P.; Zhang, H. The chemistry of two-dimensional layered transition metal dichalcogenide nanosheets. *Nat. Chem.* **2013**, *5*, 263–275.
4. Zeng, M.; Xiao, Y.; Liu, J.; Yang, K.; Fu, L. Exploring two-dimensional materials toward the next-generation circuits: from monomer design to assembly control. *Chem. Rev.* **2018**, *118*, 6236–6296.
5. Li, Y.; Sun, L.; Chang, Z.; Liu, H.; Wang, Y.; Liang, Y.; Chen, B.; Ding, Q.; Zhao, Z.; Wang, R.; Wei, Y.; Peng, H.; Lin, L.; Liu, Z. Large single-crystal Cu foils with high-index facets by strain-engineered anomalous grain growth. *Adv. Mater.* **2020**, *32*, 2002034.
6. Rickhaus, P.; Liu, M.-H.; Kurpas, M.; Kurzmann, A.; Lee, Y.; Overweg, H.; Eich, M.; Pisoni, R.; Taniguchi, T.; Watanabe, K.; Richter, K.; Ensslin, K.; Ihn, T. The electronic thickness of graphene. *Sci. Adv.* **2020**, *6*, eaay8409.
7. Zhang, Y.; Chang, T.-R.; Zhou, B.; Cui, Y.-T.; Yan, H.; Liu, Z.; Schmitt, F.; Lee, J.; Moore, R.; Chen, Y.; Lin, H.; Jeng, H.-T.; Mo, S.-K.; Hussain, Z.; Bansil, A.; Shen, Z.-X. Direct observation of the transition from indirect to direct bandgap in atomically thin epitaxial MoSe₂. *Nat. Nanotechnol.* **2014**, *9*, 111–115.

8. Ganatra, R.; Zhang, Q. Few-layer MoS₂: a promising layered semiconductor. *ACS Nano* **2014**, *8*, 4074–4099.
9. Li, X.; Zhu, H. Two-dimensional MoS₂: Properties, preparation, and applications. *J. Materiomics* **2015**, *1*, 33–44.
10. Eftekhari, A. Molybdenum diselenide (MoSe₂) for energy storage, catalysis, and optoelectronics. *Appl. Mater. Today* **2017**, *8*, 1–17.
11. Wu, X.; Wang, Y.-h.; Li, P.-l.; Xiong, Z.-z. Research status of MoSe₂ and its composites: a review. *Superlattices Microstruct.* **2020**, *139*, 106388.
12. Jaramillo, T. F.; Jørgensen, K. P.; Bonde, J.; Nielsen, J. H.; Horch, S.; Chorkendorff, I. Identification of active edge sites for electrochemical H₂ evolution from MoS₂ nanocatalysts. *Science* **2007**, *317*, 100–102.
13. Mas-Balleste, R.; Gomez-Navarro, C.; Gomez-Herrero, J.; Zamora, F. 2D materials: to graphene and beyond. *Nanoscale* **2011**, *3*, 20–30.
14. Gupta, A.; Sakthivel, T.; Seal, S. Recent development in 2D materials beyond graphene. *Prog. Mater. Sci.* **2015**, *73*, 44–126.
15. Tang, L.; Tan, J.; Nong, H.; Liu, B.; Cheng, H.-M. Chemical vapor deposition growth of two-dimensional compound materials: controllability, material quality, and growth mechanism. *Acc. Mater. Res.* **2021**, *2*, 36–47.
16. Lin, Z.; Liu, Y.; Halim, U.; Ding, M.; Liu, Y.; Wang, Y.; Jia, C.; Chen, P.; Duan, X.; Wang, C.; Song, F.; Li, M.; Wan, C.; Huang, Y.; Duan, X. Solution-processable 2D semiconductors for high-performance large-area electronics. *Nature* **2018**, *562*, 254–258.
17. Gao, Q.; Zhang, Z.; Xu, X.; Song, J.; Li, X.; Wu, Y. Scalable high performance radio frequency electronics based on large domain bilayer MoS₂. *Nat. Commun.* **2018**, *9*, 4778.

18. Zhang, Y.; Ji, Q.; Han, G.-F.; Ju, J.; Shi, J.; Ma, D.; Sun, J.; Zhang, Y.; Li, M.; Lang, X.-Y.; Zhang, Y.; Liu, Z. Dendritic, transferable, strictly monolayer MoS₂ flakes synthesized on SrTiO₃ single crystals for efficient electrocatalytic applications. *ACS Nano* **2014**, *8*, 8617–8624.
19. Ye, G.; Gong, Y.; Lin, J.; Li, B.; He, Y.; Pantelides, S. T.; Zhou, W.; Vajtai, R.; Ajayan, P. M. Defects engineered monolayer MoS₂ for improved hydrogen evolution reaction. *Nano Lett.* **2016**, *16*, 1097–1103.
20. Liu, Y.; Huang, Y.; Duan, X. Van der Waals integration before and beyond two-dimensional materials. *Nature* **2019**, *567*, 323–333.
21. Zhang, R.; Li, M.; Li, L.; Wei, Z.; Jiao, F.; Geng, D.; Hu, W. The more, the better—recent advances in construction of 2D multi-heterostructures. *Adv. Funct. Mater.* **2021**, *31*, 2102049.
22. Wang, Y.; Kim, J. C.; Wu, R. J.; Martinez, J.; Song, X.; Yang, J.; Zhao, F.; Mkhoyan, A.; Jeong, H. Y.; Chhowalla, M. Van der Waals contacts between three-dimensional metals and two-dimensional semiconductors. *Nature* **2019**, *568*, 70–74.
23. Liu, X.; Hersam, M. C. Interface characterization and control of 2D materials and heterostructures. *Adv. Mater.* **2018**, *30*, 1801586.
24. Schneider, D. S.; Lucchesi, L.; Reato, E.; Wang, Z.; Piacentini, A.; Bolten, J.; Mariani, D.; Marin, E. G.; Radenovic, A.; Wang, Z.; Fiori, G.; Kis, A.; Iannaccone, G.; Neumaier, D.; Lemme, M. C. CVD graphene contacts for lateral heterostructure MoS₂ field effect transistors. *npj 2D Mater. Appl.* **2024**, *8*, 35.
25. Behranginia, A.; Yasaei, P.; Majee, A. K.; Sangwan, V. K.; Long, F.; Foss, C. J.; Foroozan, T.; Fuladi, S.; Hantehzadeh, M. R.; Shahbazian-Yassar, R.; Hersam, M. C.; Aksamija, Z.; Salehi-Khojin, A. Direct growth of high mobility and low-noise lateral MoS₂-Graphene heterostructure electronics. *Small* **2017**, *13*, 1604301.

26. Liu, X.; Wu, Q.; Dai, M.; Xu, Q.; Zhang, X.; Cai, Z.; Ostrikov, K. K.; Gu, X.; Nan, H.; Xiao, S. Controllable one-pot growth of MoSe₂/WSe₂ lateral and vertical heterostructures by facile chemical vapor deposition. *ACS Appl. Electron. Mater.* **2023**, *5*, 5494–5502.
27. Hoang, A. T.; Hu, L.; Katiyar, A. K.; Ahn, J.-H. Two-dimensional layered materials and heterostructures for flexible electronics. *Matter* **2022**, *5*, 4116–4132.
28. Liu, X.; Hersam, M. C. Borophene-graphene heterostructures. *Sci. Adv.* **2019**, *5*, eaax6444.
29. Duan, X.; Wang, C.; Shaw, J. C.; Cheng, R.; Chen, Y.; Li, H.; Wu, X.; Tang, Y.; Zhang, Q.; Pan, A.; Jiang, J.; Yu, R.; Huang, Y.; Duan, X. Lateral epitaxial growth of two-dimensional layered semiconductor heterojunctions. *Nat. Nanotechnol.* **2014**, *9*, 1024–1030.
30. Chen, X.; Qiu, Y.; Yang, H.; Liu, G.; Zheng, W.; Feng, W.; Cao, W.; Hu, W.; Hu, P. In-plane mosaic potential growth of large-area 2D layered semiconductors MoS₂-MoSe₂ lateral heterostructures and photodetector application. *ACS Appl. Mater. Interfaces* **2017**, *9*, 1684–1691.
31. Barik, G.; Pal, S. 2D MoS₂-MoSe₂ and MoS₂-NbS₂ lateral heterostructures as anode materials for LIBs/SIBs. *Appl. Surf. Sci.* **2022**, *596*, 153529.
32. Darboe, A. K.; Qi, X.; Gong, X.; Peng, Q.; Chen, Y.; Xie, R.; Zhong, W.; Wu, G. Constructing MoSe₂/MoS₂ and MoS₂/MoSe₂ inner and outer-interchangeable flower-like heterojunctions: a combined strategy of interface polarization and morphology configuration to optimize microwave absorption performance. *J. Colloid Interface Sci.* **2022**, *624*, 204–218.
33. Bellus, M. Z.; Mahjouri-Samani, M.; Lane, S. D.; Oyedele, A. D.; Li, X.; Poretzky, A. A.;

- Geohegan, D.; Xiao, K.; Zhao, H. Photocarrier transfer across monolayer MoS₂-MoSe₂ lateral heterojunctions. *ACS Nano* **2018**, *12*, 7086–7092.
34. Jia, P.-Z.; Zeng, Y.-J.; Wu, D.; Pan, H.; Cao, X.-H.; Zhou, W.-X.; Xie, Z.-X.; Zhang, J.-X.; Chen, K.-Q. Excellent thermoelectric performance induced by interface effect in MoS₂/MoSe₂ van der Waals heterostructure. *J. Phys.:Condens. Matter* **2019**, *32*, 055302.
35. Xu, S.; Wu, P.; Chen, Y. Interfacial thermal conductance in 2D WS₂/MoSe₂ and MoS₂/MoSe₂ lateral heterostructures. *Comput. Mater. Sci.* **2024**, *245*, 113282.
36. Liang, L.; Meunier, V. First-principles Raman spectra of MoS₂, WS₂ and their heterostructures. *Nanoscale* **2014**, *6*, 5394–5401.
37. Yang, J.; Yao, H. Automated identification and characterization of two-dimensional materials via machine learning-based processing of optical microscope images. *Extreme Mech. Lett.* **2020**, *39*, 100771.
38. Li, Y.; Kong, Y.; Peng, J.; Yu, C.; Li, Z.; Li, P.; Liu, Y.; Gao, C.-F.; Wu, R. Rapid identification of two-dimensional materials via machine learning assisted optic microscopy. *J. Materiomics* **2019**, *5*, 413–421.
39. Masubuchi, S.; Machida, T. Classifying optical microscope images of exfoliated graphene flakes by data-driven machine learning. *npj 2D Mater. Appl.* **2019**, *3*, 4.
40. Ryu, B.; Wang, L.; Pu, H.; Chan, M. K. Y.; Chen, J. Understanding, discovery, and synthesis of 2D materials enabled by machine learning. *Chem. Soc. Rev.* **2022**, *51*, 1899–1925.
41. Lu, B.; Xia, Y.; Ren, Y.; Xie, M.; Zhou, L.; Vinai, G.; Morton, S. A.; Wee, A. T. S.; van der Wiel, W. G.; Zhang, W.; Wong, P. K. J. When machine learning meets 2D materials: a review. *Adv. Sci.* **2024**, *11*, 2305277.

42. Si, Z.; Zhou, D.; Yang, J.; Lin, X. Review: 2D material property characterizations by machine-learning-assisted microscopies. *Appl. Phys. A* **2023**, *129*, 248.
43. Choudhary, K.; DeCost, B.; Chen, C.; Jain, A.; Tavazza, F.; Cohn, R.; Park, C. W.; Choudhary, A.; Agrawal, A.; Billinge, S. J.; Holm, E.; Ong, S. P.; Wolverton, C. Recent advances and applications of deep learning methods in materials science. *npj Comput. Mater.* **2022**, *8*, 59.
44. Dong, X.; Li, H.; Yan, Y.; Cheng, H.; Zhang, H. X.; Zhang, Y.; Le, T. D.; Wang, K.; Dong, J.; Jakobi, M.; Yetisen, A. K.; Koch, A. W. Deep-learning-based microscopic imagery classification, segmentation, and detection for the identification of 2D semiconductors. *Adv. Theor. Simul.* **2022**, *5*, 2200140.
45. He, J.; Zhou, Y.; Zhang, P.; Zhai, H. Machine learning assisted fast optical identification of 2D materials. *Appl. Surf. Sci.* **2024**, *686*, 162110.
46. Masubuchi, S.; Watanabe, E.; Seo, Y.; Okazaki, S.; Sasagawa, T.; Watanabe, K.; Taniguchi, T.; Machida, T. Deep-learning-based image segmentation integrated with optical microscopy for automatically searching for two-dimensional materials. *npj 2D Mater. Appl.* **2020**, *4*, 3.
47. Dong, X.; Li, H.; Jiang, Z.; Grünleitner, T.; Güler, I.; Dong, J.; Wang, K.; Köhler, M. H.; Jakobi, M.; Menze, B. H.; Yetisen, A. K.; Sharp, I. D.; Stier, A. V.; Finley, J. J.; Koch, A. W. 3D deep learning enables accurate layer mapping of 2D materials. *ACS Nano* **2021**, *15*, 3139–3151.
48. Shi, C.; Cao, M. C.; Rehn, S. M.; Bae, S.-H.; Kim, J.; Jones, M. R.; Muller, D. A.; Han, Y. Uncovering material deformations via machine learning combined with four-dimensional scanning transmission electron microscopy. *npj Comput. Mater.* **2022**, *8*, 114.

49. Yang, H.; Hu, R.; Wu, H.; He, X.; Zhou, Y.; Xue, Y.; He, K.; Hu, W.; Chen, H.; Gong, M.; Zhang, X.; Tan, P.-H.; Hernández, E. R.; Xie, Y. Identification and structural characterization of twisted atomically thin bilayer materials by deep learning. *Nano Lett.* **2024**, *24*, 2789–2797.
50. Zhu, L.; Tang, J.; Li, B.; Hou, T.; Zhu, Y.; Zhou, J.; Wang, Z.; Zhu, X.; Yao, Z.; Cui, X.; Watanabe, K.; Taniguchi, T.; Li, Y.; Han, Z. V.; Zhou, W.; Huang, Y.; Liu, Z.; Hone, J. C.; Hao, Y. Artificial neuron networks enabled identification and characterizations of 2D Materials and van der Waals heterostructures. *ACS Nano* **2022**, *16*, 2721–2729.
51. Lin, X.; Si, Z.; Fu, W.; Yang, J.; Guo, S.; Cao, Y.; Zhang, J.; Wang, X.; Liu, P.; Jiang, K.; Zhao, W. Intelligent identification of two-dimensional nanostructures by machine-learning optical microscopy. *Nano Res.* **2018**, *11*, 6316–6324.
52. Bhawsar, S.; Fang, M.; Sarkar, A. S.; Chen, S.; Yang, E.-H. Deep learning-based multimodal analysis for transition-metal dichalcogenides. *MRS Bull.* **2024**, 1–11.
53. Chen, T.; Ding, D.; Shi, J.; Wang, G.; Kou, L.; Zheng, X.; Ren, X.; Liu, X.; Jin, C.; Zhong, J.; Hao, G. Lateral and vertical MoSe₂-MoS₂ heterostructures via epitaxial growth: triggered by high-temperature annealing and precursor concentration. *J. Phys. Chem. Lett.* **2019**, *10*, 5027–5035.
54. Wang, S.; Rong, Y.; Fan, Y.; Pacios, M.; Bhaskaran, H.; He, K.; Warner, J. H. Shape evolution of monolayer MoS₂ crystals grown by chemical vapor deposition. *Chem. Mater.* **2014**, *26*, 6371–6379.
55. Cao, D.; Shen, T.; Liang, P.; Chen, X.; Shu, H. Role of chemical potential in flake shape and edge properties of monolayer MoS₂. *J. Phys. Chem C* **2015**, *119*, 4294–4301.
56. Wang, L.; Chen, F.; Ji, X. Shape consistency of MoS₂ flakes grown using chemical vapor deposition. *Appl. Phys. Express* **2017**, *10*, 065201.

57. Cho, Y. J.; Sim, Y.; Lee, J.-H.; Hoang, N. T.; Seong, M.-J. Size and shape control of CVD-grown monolayer MoS₂. *Curr. Appl. Phys.* **2023**, *45*, 99–104.
58. Moses, I. A.; Reinhart, W. F. Quantitative analysis of MoS₂ thin film micrographs with machine learning. *Mater. Charact.* **2024**, *209*, 113701.
59. Cai, Y.; Xu, K.; Zhu, W. Synthesis of transition metal dichalcogenides and their heterostructures. *Mater. Res. Express* **2018**, *5*, 095904.
60. Wang, Z.; Xie, Y.; Wang, H.; Wu, R.; Nan, T.; Zhan, Y.; Sun, J.; Jiang, T.; Zhao, Y.; Lei, Y.; Yang, M.; Wang, W.; Zhu, Q.; Ma, X.; Hao, Y. NaCl-assisted one-step growth of MoS₂–WS₂ in-plane heterostructures. *Nanotechnology* **2017**, *28*, 325602.